J|A|C|S

A R T I C L E S

Manganese Oxides: Parallels between Abiotic and Biotic Structures

Ian Saratovsky,[†,#] Peter G. Wightman,[#,‡] Pablo A. Pastén,[§]
Jean-François Gaillard,[#,‡] and Kenneth R. Poeppelmeier*,[†,#]

*Contribution from the Department of Chemistry and Department of Environmental Engineering
and Science, Northwestern University, Evanston, Illinois 60208, Institute for Environmental
Catalysis, Northwestern University, Evanston, Illinois 60618, and Departamento de Ingeniería
Hidráulica y Ambiental, Pontifica Universidad Católica de Chile, Santiago, Código Postal
6904411, Chile*

Received March 27, 2006; E-mail: krp@northwestern.edu

Abstract: A large number of microorganisms are responsible for the oxidation of $Mn^{2+}_{(aq)}$ to insoluble $Mn^{3+/4+}$ oxides (MnO_x) in natural aquatic systems. This paper reports the structure of the biogenic MnO_x, including a quantitative analysis of cation vacancies, formed by the freshwater bacterium *Leptothrix discophora* SP6 (SP6-MnO_x). The structure and the morphology of SP6-MnO_x were characterized by transmission electron microscopy (TEM), X-ray absorption spectroscopy (XAS), including full multiple-scattering analysis, and powder X-ray diffraction (XRD). The biogenic precipitate consists of nanoparticles that are approximately 10 nm by 100 nm in dimension with a fibrillar morphology that resembles twisted sheets. The results demonstrate that this biogenic MnO_x is composed of sheets of edge-sharing of $Mn^{4+}O_6$ octahedra that form layers. The detailed analysis of the EXAFS spectra indicate that $12 \pm 4\%$ of the Mn^{4+} layer cation sites in SP6-MnO_x are vacant, whereas the analysis of the XANES suggests that the average oxidation state of Mn is 3.8 ± 0.3. Therefore, the average chemical formula of SP6-MnO_x is $M^{n+}_y Mn^{3+}_{0.12}[\square_{0.12}Mn^{4+}_{0.88}]O_2 \cdot zH_2O$, where M^{n+}_y represents hydrated interlayer cations, $\square_{0.12}$ represents Mn^{4+} cation vacancies within the layer, and $Mn^{3+}_{0.12}$ represents hydrated cations that occupy sites above/below these cation vacancies.

Introduction

Manganese oxides (MnO_x) with layered topologies are ubiquitous in industry and throughout the natural environment. The importance of these materials in industrial applications and natural systems stems from the variability of several key structural parameters that influence their properties. The porosity, degree of interlayer hydration, average manganese oxidation state, and presence/quantity of cation vacancies within the layer can all vary and determine specific materials properties. Layered MnO_x are utilized currently in Li^+ ion battery cathodes,[1–4] taking advantage of high surface areas derived from porosity and small particle sizes.[5] Other applications of MnO_x[6–11] exploit

the mixed oxidation states of manganese (3+ and 4+). The cation vacancies within MnO_x layers create negative charge,[12–16] providing a driving force for cation intercalation[17,18] and cation sorption.[19–24] Consequently, these oxides have potential applications in the environmental remediation of metals.[25–30] The

† Department of Chemistry, Northwestern University.
# Institute for Environmental Catalysis, Northwestern University.
‡ Department of Environmental Engineering and Science, Northwestern University.
§ Pontifica Universidad Católica de Chile.

(1) Whittingham, M. S.; Zavalij, P. Y. *Solid State Ionics* **2000**, *131*, 109–115.
(2) Whittingham, M. S.; Zavalij, P.; Zhang, F.; Sharma, P.; Moore, G. In *The Stabilization of Layered Manganese Oxides for Use in Eecharegable Lithium Batteries*; Materials Research Society Symposium Proceedings; Materials Research Society: Warrendale, PA, 2000; pp 77–82.
(3) Whittingham, M. S.; Zavalij, P.; Ngala, K. In *Pillared Oxides of Manganese and Vanadium for Lithium Batteries—Geometric and Electronic Factors*; Proceedings; Electrochemical Society: Pennington, NJ, 2001; pp 8–17.
(4) Whittingham, M. S. *Chem. Rev.* **2004**, *104*, 4271–4301.
(5) Kim, S. H.; Kim, S. J.; Oh, S. M. *Chem. Mater.* **1999**, *11*, 557–563.
(6) Wang, Y.; Ohtsuka, Y. *Top. Catal.* **2003**, *22*, 71–75.
(7) Alvarez-Galvan, M. C.; de la Pena O'Shea, V. A.; Fierro, J. L. G.; Arias, P. L. *Catal. Commun.* **2003**, *4*, 223–228.
(8) Brueckner, A.; Bentrup, U.; Radnik, J.; Richter, M.; Fricke, R. *Stud. Surf. Sci. Catal.* **2003**, *145*, 463–464.
(9) Chen, A.; Xu, H.; Yue, Y.; Hua, W.; Shen, W.; Gao, Z. *J. Mol. Catal. A: Chem.* **2003**, *203*, 299–306.
(10) Jokic, A.; Frenkel, A. I.; Vairavamurthy, M. A.; Huang, P. M. *Geophys. Res. Lett.* **2001**, *28*, 3899–3902.
(11) Liu, J.; Cai, J.; Son, Y. C.; Gao, Q. M.; Suib, S. L.; Aindow, M. *J. Phys. Chem. B* **2002**, *106*, 9761–9768.
(12) Giovanoli, R.; Stahli, E.; Feitknecht, W. *Helv. Chim. Acta* **1970**, *53*, 209.
(13) Giovanoli, R.; Stahli, E.; Feitknecht, W. *Helv. Chim. Acta* **1970**, *53*, 453.
(14) Manceau, A.; Combes, J. M. *Phys. Chem. Miner.* **1988**, *15*, 283–295.
(15) Manceau, A.; Gorshkov, A. I.; Drits, V. A. *Am. Mineral.* **1992**, *77*, 1144–1157.
(16) Manceau, A.; Gorshkov, A. I.; Drits, V. A. *Am. Mineral.* **1992**, *77*, 1133–1143.
(17) Gao, Q.; Giraldo, O.; Tong, W.; Suib, S. L. *Chem. Mater.* **2001**, *13*, 778–786.
(18) Means, J. L.; Crerar, D. A.; Borcsik, M. P.; Duguid, J. O. *Geochim. Cosmochim. Acta* **1978**, *42*, 1763–1773.
(19) Matocha, C. J.; Elzinga, E. J.; Sparks, D. L. *Environ. Sci. Technol.* **2001**, *35*, 2967–2972.
(20) Toner, B.; Manceau, A.; Marcus, M. A.; Millet, D. B.; Sposito, G. *Environ. Sci. Technol.* **2005**, *39*, 8288–8294.
(21) Lanson, B.; Drits, V. A.; Gaillot, A. C.; Silvester, E.; Plancon, A.; Manceau, A. *Am. Mineral.* **2002**, *87*, 1631–1645.
(22) Drits, V. A.; Lanson, B.; Bougerol-Chaillout, C.; Gorshkov, A. I.; Manceau, A. *Am. Mineral.* **2002**, *87*, 1646–1661.
(23) Manceau, A.; Lanson, B.; Drits, V. A. *Geochim. Cosmochim. Acta* **2002**, *66*, 2639–2663.
(24) Manceau, A.; Drits, V. A.; Silvester, E.; Bartoli, C.; Lanson, B. *Am. Mineral.* **1997**, *82*, 1150–1175.

variability in structural and electronic parameters of MnO_x plays a determining role in the transport, speciation, and ultimate fate of metals and natural organic matter in the natural environment.[31]

Most natural manganese oxides formed at low temperature result from microbially mediated oxidation of aqueous Mn^{2+}.[32−34] In natural systems Mn^{2+}, Mn^{3+}, and Mn^{4+} are the most favored oxidation states,[35] of which only Mn^{2+} and complexed Mn^{3+} are soluble in water.[36,37] Therefore, the formation of Mn^{3+}/Mn^{4+} oxides proceeds by oxidation of aqueous Mn^{2+} ions, a thermodynamically favorable but kinetically slow reaction.[36,38,39] Consequently, the oxidation of aqueous Mn^{2+} must be catalyzed owing to the scarcity of sufficiently strong oxidants in natural systems. In the environment, this catalytic role is filled by a class of microorganisms collectively referred to as "manganese oxidizers".[32,40]

Detailed knowledge of MnO_x structures formed by microorganisms living in a variety of environmental conditions can provide insight into their biological importance and how they ultimately affect the speciation of otherwise mobile organic compounds and metals. Within the past several years, the structures of the MnO_x formed by the spore-forming marine *Bacillus* sp. strain SG-1[41,42] and *Pseudomonas putida* strain MnB1[43] bacteria have been investigated in great detail and successfully identified. These distinct bacteria species produce similar mixed-valent, layered $Mn^{3+/4+}O_x$. Additionally, the structure of MnO_x formed by the freshwater bacterium *Leptothrix discophora* SP6 (SP6-MnO_x) has been reported by Kim et al.[44,45] and Juergensen et al.[46] Disagreement exists on the basic atomic structure of SP6-MnO_x. Kim et al.[44,45] reported that the SP6-MnO_x UV Raman spectrum closely resembles a todorokite-like tunnel structure,

whereas Juergensen and co-workers[46] concluded that SP6-MnO_x possesses a layered topology.

In this work, we report a detailed investigation of the structure of biogenic MnO_x as well as abiotic counterparts. In addition, we propose a quantitative analysis of metal cation vacancies. The detailed structure resolution was performed by a combination of X-ray absorption spectroscopy (XAS), including full multiple-scattering analysis and powder X-ray diffraction (XRD). Particle morphology was investigated by transmission electron microscopic (TEM) imaging. The structure of biogenic MnO_x was elucidated by spectroscopic comparison to a variety of synthetic MnO_x phases for which detailed structures are known. Moreover, this biogenic MnO_x was characterized in its near-natural, hydrated state, not in a dried form that may alter the structure of metastable phases.[47] The existence and quantity of cation vacancies in abiotic layered MnO_x have been matters of dispute within the literature,[48] and their investigation previously has been limited to cases in which highly crystalline materials can be formed. In this work, we propose an EXAFS-based method that uses local structure information to quantify the number of metal cation vacancies in poorly ordered MnO_x precipitates by comparison to crystalline, abiotic reference materials.

Experimental Section

Growth of *L. discophora* SP6 and Biogenic MnO_x Production. A frozen stock culture of *L. discophora* SP-6 (ATCC 51168) was obtained from American Type Culture Collection (ATCC).[49,50] Liquid cultures of SP-6 were grown in mineral salts, vitamins, and pyruvate (MSVP)/noFe, a modified version of the MSVP medium (ATTCC Culture Medium 1917) used by Emerson and Ghiorse.[49,50] The difference between MSVP/noFe and MSVP was that $FeSO_4$ was not added to MSVP/noFe. Iron was limited to ensure slow bacterial growth conditions that promote sheath formation and consequent $Mn^{2+}_{(aq)}$ oxidizing capability.[49,50] In addition, the presence of Fe^{2+} in the medium can lead to the incorporation of iron within the MnO_x structure and can complicate matters.[29] All cultures were maintained aerobically at room temperature (~25 °C), except for the SP-6 stock cultures (frozen stocks were maintained at ~ -85 °C). Liquid cultures were stirred slowly (<100 rpm) on a shaker table.

Biomass in liquid cultures was measured by absorbance at 600 nm, according to the spectrophotometric method used by Emerson.[49] Light microscopy was used to confirm the presence of sheaths and the characteristic morphological traits of SP-6. The SP6-MnO_x was produced by growing a liquid culture of SP-6 in MSVP/noFe to stationary phase. Under these conditions, Fe is considered the limiting growth factor. A total of 62.5 mL of a 20 mM $Mn^{2+}_{(aq)}$ stock solution was added to the 5 L SP-6 culture to obtain a final concentration of $[Mn^{2+}] = 250 \ \mu M$.[51]

Binary MnO_x Reference Materials. MnO, Mn_2O_3, and β-MnO_2 (pyrolusite) were purchased from Aldrich, and phase purities were confirmed by powder X-ray diffraction.

Synthesis of *c*-Ordered Hexagonal K^+-Birnessite. This compound was synthesized by the thermal decomposition of $KMnO_4$ at 800 °C for 16 h.[5] Five grams of $KMnO_4$ was heated at 2 °C/min to 800 °C,

(25) Taillefert, M.; MacGregor, B. J.; Gaillard, J. F.; Lienemann, C. P.; Perret, D.; Stahl, D. A. *Environ. Sci. Technol.* **2002**, *36*, 468−476.
(26) Dyer, A.; Pillinger, M.; Newton, J.; Harjula, R.; Moeller, T.; Amin, S. *Chem. Mater.* **2000**, *12*, 3798−3804.
(27) Al-Attar, L.; Dyer, A. *J. Mater. Chem.* **2002**, *12*, 1381−1386.
(28) Katsoyiannis, I. A.; Zouboulis, A. I.; Jekel, M. *Ind. Eng. Chem. Res.* **2004**, *43*, 486−493.
(29) Lienemann, C. P.; Taillefert, M.; Perret, D.; Gaillard, J. F. *Geochim. Cosmochim. Acta* **1997**, *61*, 1437−1446.
(30) Webb, S. M.; Fuller, C. C.; Tebo, B. M.; Bargar, J. R. *Environ. Sci. Technol.* **2006**, *40*, 771−777.
(31) Post, J. E. *Proc. Natl. Acad. Sci. U.S.A.* **1999**, *96*, 3447−3454.
(32) Tebo, B. M.; He, L. M. Microbially mediated oxidative precipitation reactions. In *Mineral−Water Interfacial Reactions*, 1st ed.; Grundl, T., Sparks, D. L., Eds.; American Chemical Society: Washington, DC, 1998; Vol. 715, pp 393−414.
(33) Tebo, B. M.; Bargar, J. R.; Clement, B. G.; Dick, G. J.; Murray, K. J.; Parker, D.; Verity, R.; Webb, S. M. *Annu. Rev. Earth Planet. Sci.* **2004**, *32*, 287−328.
(34) Tebo, B. M.; Ghiorse, W. C.; Van Waasbergen, L. G.; Siering, P. L.; Caspi, R. *Rev. Mineral.* **1997**, *35*, 225−266.
(35) Frost, A. A. *J. Am. Chem. Soc.* **1951**, *73*, 2680−2682.
(36) Morgan, J. J. *Geochim. Cosmochim. Acta* **2004**, *69*, 35−48.
(37) Klewicki, J. K.; Morgan, J. J. *Environ. Sci. Technol.* **1998**, *32*, 2916−2922.
(38) Stumm, W.; Morgan, J. J. *Aquatic Chemistry: Chemical Equilibria and Rates in Natural Waters*, 3rd ed.; Wiley: New York, 1996; p 1022.
(39) Luther III, G. W. In *Aquatic Chemical Kinetics: Reaction Rates of Processes in Natural Waters*; Stumm, W., Metcalf, R. L., Eds.; Wiley-Interscience: New York, 1990; pp 173−198.
(40) Emerson, S.; Kalhorn, S.; Jacobs, L.; Tebo, B. M.; Nealson, K. H.; Rosson, R. A. *Geochim. Cosmochim. Acta* **1982**, *46*, 1073−1079.
(41) Webb, S. M.; Tebo, B. M.; Bargar, J. R. *Am. Mineral.* **2005**, *90*, 1342−1357.
(42) Bargar, J. R.; Tebo, B. M.; Bergmann, U.; Webb, S. M.; Glatzel, P.; Chiu, V. Q.; Villalobos, M. *Am. Mineral.* **2005**, *90*, 143−154.
(43) Villalobos, M.; Toner, B.; Bargar, J.; Sposito, G. *Geochim. Cosmochim. Acta* **2003**, *67*, 2649−2662.
(44) Kim, H.-S.; Pasten, P. A.; Gaillard, J.-F.; Stair, P. C. *J. Am. Chem. Soc.* **2003**, *125*, 14284−14285.
(45) Kim, H. S.; Stair, P. C. *J. Phys. Chem. B* **2004**, *108*, 17019−17026.
(46) Juergensen, A.; Widmeyer, J. R.; Gordon, R. A.; Bendell-Young, L. I.; Moore, M. M.; Crozier, E. D. *Am. Mineral.* **2004**, *89*, 1110−1118.

(47) Fritsch, S.; Post, J. E.; Suib, S. L.; Navrotsky, A. *Chem. Mater.* **1998**, *10*, 474−479.
(48) Yang, D. S.; Wang, M. K. *Chem. Mater.* **2001**, *13*, 2589−2594.
(49) Emerson, D. Ultrastructural organization, chemical composition, and manganese-oxidizing properties of the sheath of *Leptothrix discophora* SP-6. Ph.D. Dissertation, Cornell University, Ithaca, NY, 1989.
(50) Emerson, D.; Ghiorse, W. C. *Appl. Environ. Microbiol.* **1992**, *58*, 4001−4010.
(51) Pasten, P. A. Structure and formation kinetics of manganese oxides by *Leptothrix discophora* SP-6. Ph.D. dissertation, Northwestern University, Evanston, IL, 2002.

maintained at 800 °C for 16 h, and cooled at 1 °C/min to room temperature to promote crystallization. The product was washed 7−10 times with 18 MΩ Milli-Q (MQ) water, until the filtrate became clear, to remove soluble manganese species with oxidation states >4.

Synthesis of c-Disordered Hexagonal H$^+$-Birnessite. This synthesis was adapted from that of McKenzie and McMurdie.[52−54] KMnO$_4$ (1.5803 g) was dissolved in 100 mL of MQ water; 1.64 mL of concentrated HCl was added dropwise to the 0.10 M KMnO$_4$ solution. Note: This reaction should be performed in a fume hood as *copious amounts of Cl$_{2(g)}$ are released!* The precipitate was collected by vacuum filtration through a fine-pored glass frit and divided into two dialysis tubes. Each dialysis tube was submerged in ∼5 L of MQ water and stirred for 24 h. The water was changed four times to ensure complete dialysis of free ions. The dialyzed precipitate was dried for 12 h at 40 °C.

Synthesis of Todorokite-like Mg^{2+}-OMS-1. Mg^{2+}-OMS-1 was synthesized using a two-step procedure adapted from that of Malinger and Suib.[55] First, a Na$^+$-birnessite precursor (Na$^+$-OL-1) was synthesized by the oxidation of Mn$^{2+}_{(aq)}$ by KMnO$_4$ in sodium hydroxide solution, and 0.5058 g of KMnO$_4$ (3.2 mmol) was added to a 3 M NaOH (∼35 mL) solution. The solution was stirred and heated at 50 °C for 1 h. A solution of 0.3200 g of MgCl$_2$ (3.4 mmol) and 1.3610 g of MnSO$_4$ (9 mmol) dissolved in 35 mL of MQ H$_2$O was added dropwise to the KMnO$_4$/NaOH solution. The resultant brown suspension was sealed in an amber bottle and aged at 50 °C for 24 h in a convection oven, resulting in the formation of Na$^+$-OL-1. Na^{+-}OL-1 was then washed 10 times with MQ H$_2$O and transferred into a 125 mL Teflon-lined Parr autoclave with ∼83 mL of 1 M MgCl$_2$ solution and treated hydrothermally at 125 °C for 48 h. After slow cooling (0.1 °C/min) to room temperature, the resulting suspension was filtered and washed several times with 150 mL of 100 °C MQ water and dried at 40 °C.

Synthesis of CaMnO$_3$ and Ca$_2$Mn$_3$O$_8$. The carbonate precursor technique for the syntheses of CaMnO$_3$ and Ca$_2$Mn$_3$O$_8$ was adapted from that of Horowitz and Longo.[56] Polycrystalline Ca$_2$Mn$_3$O$_8$ was identified on the basis of the crystal structure determined by Poeppelmeier and co-workers.[57] Stoichiometric quantities of CaCO$_3$ and MnCO$_3$ were dissolved in dilute nitric acid. MnCO$_3$ should be freshly prepared and stored under vacuum until needed. Commercially available MnCO$_3$ was found to be oxidized, as evidenced by brown color, and was not used. MnCO$_3$ was prepared by dissolution of Mn(NO$_3$)$_2$ in MQ H$_2$O, followed by precipitation with excess (NH$_4$)$_2$CO$_3$. In a typical synthesis of Ca$_2$Mn$_3$O$_8$ 0.4424 g of CaCO$_3$ (4.42 mmol) and 0.7616 g of MnCO$_3$ (6.63 mmol) were dissolved in 250 mL of acidified MQ H$_2$O. A 10-fold molar excess of dissolved (NH$_4$)$_2$CO$_3$ was added to precipitate the Ca$_2$Mn$_3$(CO$_3$)$_5$ solid solution. The Ca$_2$Mn$_3$(CO$_3$)$_5$ solid solution was dried at 100 °C under vacuum. Ca$_2$Mn$_3$O$_8$ was formed by calcination and oxidation of Ca$_2$Mn$_3$(CO$_3$)$_5$ for 5 h at 800 °C under flowing O$_2$ with one intermediate regrind. CaMnO$_3$ synthesis follows the same reaction scheme with a 1:1 molar ratio of Ca to Mn.

Synthesis of ZnMn$_3$O$_7$·3H$_2$O (Chalcophanite). The preparation of synthetic Zn-chalcophanite was adapted from that of Stein et al.[58] The synthesis proceeds by preparation of Na$^+$-birnessite followed by cation exchange of Na$^+$ for Zn^{2+}. Eleven grams of Mn^{II}(CH$_3$COO)$_2$ (0.0636 mol) and 5.4056 g of NaNO$_3$ (0.0636 mol) were dissolved in deoxygenated MQ H$_2$O. The solution was stirred vigorously and heated at 100 °C until dry. A tan/brown powder resulted. The resultant powder

was calcined at 400 °C in air for 7 h, resulting in Na$^+$-birnessite. Na$^+$-birnessite was resuspended in a 0.66 M Zn(NO$_3$)$_2$ solution and stirred vigorously overnight and washed several times to ensure complete cation exchange. The suspension was vacuum filtered and dried at 40 °C for 5 h.

Transmission Electron Microscopy. Bacterial specimens were fixed, stained, dehydrated, embedded in resin, microtomed, and poststained. Two types of embedding were used to identify/reduce artifacts: hydrophobic epoxy embedding[59] and hydrophilic melamin embedding.[60] Epoxy embedding was achieved by glutaraldehyde fixation followed by staining with uranyl acetate, dehydration with ethanol and propylene oxide, embedding in resin, microtomy, and poststaining. Thin sections used for elemental X-ray microanalysis omitted staining for purposes of accurate determination of the elemental composition.

A modification of the method of Leppard et al.[61] was used for melamin embedding. The procedure consists of directly infiltrating *L. discophora* SP6 and associated MnO$_x$ with the melamin resin and polymerization/curing for 2 days at 40 °C in a desiccator and for 2 days at 60 °C. Owing to the brittleness of the melamin-embedded sample, an epoxy resin was used to form a composite section. A thin strip of the sample already embedded in hardened melamin resin was embedded in epoxy resin, making possible microtomy of a thin section. This method omits fixation, dehydration, and staining compared to epoxy embedding, which are deemed to be appropriate for structure imaging, but potentially interfere with MnO$_x$ microstructure visualization. Thin sections of embedded samples were collected and supported on 200 mesh Formvar-coated copper grids, obtained from SPI, Structure Probe Inc.

Transmission electron microscopy (TEM) micrographs (Figure 1a) of *L. discophora* SP6 and associated MnO$_x$ were collected on a Hitachi HF-2000 microscope equipped with a Princeton Gamma Tech X-ray detector, used for energy dispersive spectrometry (EDS). A tilt series, in which the tilt was varied between 0° and 30°, was taken using a Philips Tecnai BioTwin TEM to investigate the morphology of SP6-MnO$_x$ particles (Figure 1b). Collection of a series of TEM images with varied stage tilt angles affords information on particle morphology in three dimensions.

X-ray Absorption Spectroscopy. Biogenic MnO$_x$ samples were separated from the growth medium by centrifugation and resuspension in MQ water. The sample was washed, centrifuged, and resuspended several times to ensure removal of unoxidized, loosely bound Mn$^{2+}_{(aq)}$ remaining from the oxidation procedure. Wet samples containing bacteria and biogenic MnO$_x$ were vacuum filtered, and samples were prepared by mounting the filter paper containing the wet solid (bacteria and MnO$_x$) between pieces of Kapton tape. MnO$_x$ reference standards were prepared for transmission measurements by spreading finely ground powders between pieces of Kapton tape. Typically, four layers of powder on Kapton tape were combined to obtain a $\mu \approx 2$ and $\Delta\mu \approx 1$ and to ensure the absence of pinholes. Transmission spectra were collected at several different locations on each sample, and reproducibility ensured sample homogeneity.

X-ray absorption spectra were collected at DND-CAT (Sector 5 beamline 5BMD) of the Advanced Photon Source at the Mn K edge in transmission and fluorescence modes. A Si(111) double-crystal monochromator was used to select wavelength. Harmonics were eliminated with a flat, Rh-coated mirror with a cutoff energy of 20 keV at 3 mrad and slight detuning (90% of $I_{0,max}$). For edge energy calibration, the X-ray absorption spectrum of a reference Mn foil was collected with each sample. The metal foil edge energy was set to the first inflection point of the absorption edge, determined by the first derivative, and was set to 6539 eV.[62] The average oxidation states of MnO$_x$ compounds

(52) McKenzie, R. M. *Mineral. Mag.* **1971**, *38*, 493−502.
(53) McMurdie, H. F. *Trans. Electrochem. Soc.* **1944**, *86*, 12 pp.
(54) McMurdie, H. F.; Golovato, E. *J. Res. Natl. Bur. Stand. (U.S.)* **1948**, *41*, 589−600.
(55) Malinger, K. A.; Laubernds, K.; Son, Y.-C.; Suib, S. L. *Chem. Mater.* **2004**, *16*, 4296−4303.
(56) Ansell, G. B.; Horowitz, H. S.; Longo, J. M. *Acta Crystallogr., Sect. A: Found. Crystallogr.* **1978**, *34*, S157−S157.
(57) Poeppelmeier, K. R.; Ansell, G. B.; Modrick, M. A.; Longo, J. M.; Horowitz, H. S. *Acta Crystallogr., Sect. B: Struct. Sci.* **1982**, *38*, 1795−1797.
(58) Aronson, B. J.; Kinser, A. K.; Passerini, S.; Smyrl, W. H.; Stein, A. *Chem. Mater.* **1999**, *11*, 949−957.

(59) Hayat, M. A. *Micron Microsc. Acta* **1986**, *17*, 115−135.
(60) Frosch, D.; Westphal, C. *Electron Microsc. Rev.* **1989**, *2*, 231−255.
(61) Droppo, I. G.; Flannigan, D. T.; Leppard, G. G.; Jaskot, C.; Liss, S. N. *Appl. Environ. Microbiol.* **1996**, *62*, 3508−3515.
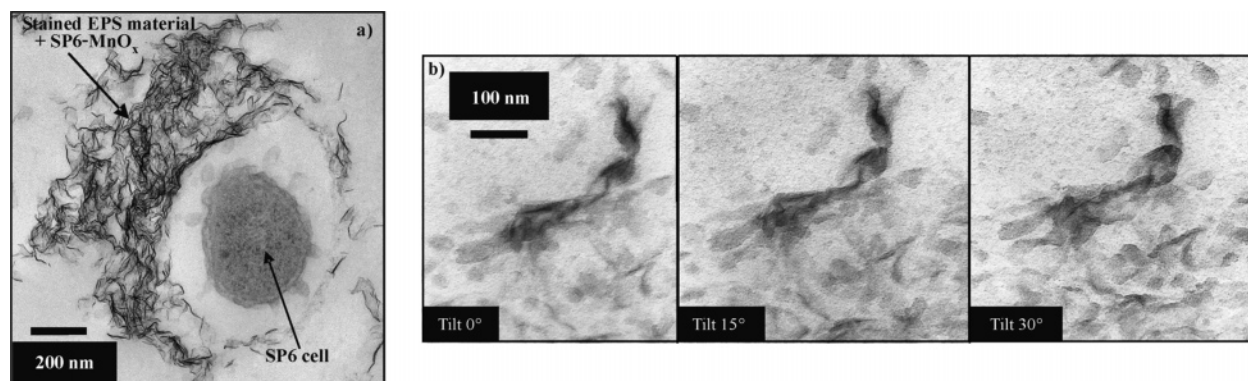
Figure 1. Morphology of SP6-MnO$_x$: (a) transmission electron micrograph of *L. discophora* SP6 that illustrates the location of the MnO$_x$ fibrils; (b) tilt series that focuses on a typical bundle of MnO$_x$ fibrils that surround *L. discophora* SP6 and illustrates twisted-sheet particle morphology.

were determined by calibration of edge energies with known oxidation states. MnO, Mn$_2$O$_3$, and MnO$_2$ were used as reference compounds for average oxidation state determination in biogenic MnO$_x$ (see Figure S1, Supporting Information).[71] Spectra of synthetic standards were collected in transmission geometry using Oxford ionization chambers with a path length of 29.6 cm. SP6-MnO$_x$ samples were measured in fluorescence yield mode. Self-absorption corrections were not necessary given the small size and dilute nature of the biogenic nanoparticles. Ionization chambers were filled with gas mixtures to obtain 10% absorption (25% N$_2$/75% He) of the incident beam in I_0, 30% absorption (75% N$_2$/25% He) in I_T (sample), and 60% absorption (95% N$_2$/5% He) in I_{T2} (reference foil). Spectra of biogenic MnO$_x$ were collected in fluorescence geometry using a Stern–Heald "Lytle" cell detector equipped with soller slits and a Z-1 filter.[63] The Lytle cell was continuously flushed with argon. For each reference MnO$_x$ and sample, nine replicate XAS spectra were collected to improve counting statistics.

A smooth atomic background was removed from each XAS spectrum, and the data were normalized to a step height of one. This is done so that E_0, the Fermi energy, can be consistently chosen as the first inflection point at the absorption edge step. E_0 is used by AutoBK[64,65] to determine the photoelectron wavenumber: $k = (2m(E - E_0)/\hbar^2)^{1/2}$, where m is the electron mass, $\hbar$ is Planck's constant, and E is the incident X-ray energy. This equation was used to convert the data from the measured EXAFS $\chi(E)$ to $\chi(k)$. The background function generated by the AutoBK algorithm[64,65] is made from third-order polynomial spline functions that are connected by knots. Similar background polynomial spline parameters were used ($R_{bkg} = 1.0$) to obtain the same background functions for all MnO$_x$ spectra. The background was removed from each data set, and then the resulting $\chi(k)$ data (nine replicates) were averaged. Processing of all XAS data was performed using SixPack,[66] Athena,[67] and Artemis[67] graphical user interfaces for XAS processing built on IFEFFIT.[67–69] Data reduction and analysis were performed using the methods of Athena and Artemis.[67] The data were fit in R-space with theoretical amplitudes and phases for single- and multiple-scattering paths that were calculated from crystal structures using the *ab initio* FEFF 8.10 code.[70] Fourier

Table 1. Abiotic Model Compounds for Spectroscopic Comparison to SP6-MnO$_x$

model compound	topology	vacancy (%)	stacking	ref
K$^+$-birnessite	layered	~12	ordered	73, 87
H$^+$-birnessite	layered	~16.7	disordered	73, 90
Zn-chalcophanite	layered	14.3	ordered	58, 81
Ca$_2$Mn$_3$O$_8$	layered	25	ordered	57
Mg-OMS1 (todorokite)	(3 × 3) tunnel	n/a	n/a	11, 92, 95

transforms were taken over similar photoelectron wavenumber ranges with the endpoints terminating at nodes, typically between 2.95 Å^{-1} ≤ k ≤ 13.35 Å^{-1}. A Kaiser–Bessel window function was used to dampen the EXAFS oscillations at endpoints. Least-squares fitting of theoretical phases and amplitudes to MnO$_x$ model compounds and biogenic MnO$_x$ were performed in Artemis.[67]

Continuous scanning XAS experiments were conducted on SP6-MnO$_x$ to ensure that beam damage to the sample did not occur.[51] The complete energy range around the Mn K edge was scanned in approximately 2 min, and replicates were collected over several hours, exhibiting no spectral change.[51,72] Therefore, it is concluded that no significant beam damage occurs to SP6-MnO$_x$. Additionally, SP6-MnO$_x$ sample spectra were collected 6 months apart to investigate the effects of aging. No changes in the SP6-MnO$_x$ spectra were witnessed after a period of 6 months.

Analysis of EXAFS: Model. The crystal structure of K$^+$-birnessite was used as a model to fit the biogenic MnO$_x$ owing to their spectral similarity. The K$^+$-birnessite spectrum was fit using a symmetrical, hexagonal layer model derived from the reported crystal structures and is illustrated in Figure 8.[73] Scattering paths up to 6 Å were generated with TkAtoms[67] using a hexagonal unit cell ($P\ 6_3$/mmc, $a = 2.840$ Å, $c = 14.50$ Å) reported by Gaillot et al.[73] FEFF 8.10 was used to calculate single- and multiple-scattering path phases and amplitudes used in the fits. The number of variables for the $k = 2.95$–13.35 Å^{-1} and $R = 0$–5.8 Å fitting range is 22, with 38 independent points, and meets the Nyquist criterion. The fit converged with goodness-of-fit parameters $R = 0.0177$ and $\chi^2 = 100.79$ (Table 2 and Figure 6). The average local environment around manganese within layered structures built up from edge-shared MnO$_6$ octahedra, up to 6 Å, was fit using a total of four Mn–O single-scattering paths, two Mn–Mn single-scattering paths, and one Mn–Mn multiple-scattering (MS) path. Nearest-neighbor coordination numbers for manganese and oxygen shells were constrained according to ideal crystallographic values with the exception of Mn^{4+}–Mn^{3+} corner-sharing octahedra at ~3.85 Å, which was allowed to float freely. S_0^2 was constrained to 0.83 derived

(62) Conradson, S. D.; Al Mahamid, I.; Clark, D. L.; Hess, N. J.; Hudson, E. A.; Neu, M. P.; Palmer, P. D.; Runde, W. H.; Tait, C. D. *Polyhedron* **1998**, *17*, 599–602.
(63) Stern, E. A.; Elam, W. T.; Bunker, B. A.; Lu, K. Q.; Heald, S. M. *Nuclear Instrum. Methods Phys. Res.* **1982**, *195*, 345–346.
(64) Newville, M.; Livins, P.; Yacoby, Y.; Rehr, J. J.; Stern, E. A. *Jpn. J. Appl. Phys., Part 1* **1993**, *32*, 125–127.
(65) Ravel, B.; Newville, M.; Cross, J. O.; Bouldin, C. E. *Physica B* **1995**, *209*, 145–147.
(66) Webb, S. M. *Phys. Scr.* **2005**, *T115*, 1011–1014.
(67) Ravel, B.; Newville, M. *J. Synchrotron Radiat.* **2005**, *12*, 537–541.
(68) Newville, M. *J. Synchrotron Radiat.* **2001**, *8*, 322–324.
(69) Newville, M. *J. Synchrotron Radiat.* **2001**, *8*, 96–100.
(70) Rehr, J. J.; Zabinsky, S. I. *FEFF5: An ab Initio Multiple Scattering XAFS Code*; Report, Department of Physics; University of Washington: Seattle, WA, 1992; 5 pp.
(71) Brock, S. L.; Sanabria, M.; Nair, J.; Suib, S. L.; Ressler, T. *J. Phys. Chem. B* **2001**, *105*, 5404–5410.

(72) Gaillard, J. F.; Webb, S. M.; Quintana, J. P. G. *J. Synchrotron Radiat.* **2001**, *8*, 928–930.
(73) Gaillot, A.-C.; Flot, D.; Drits, V. A.; Manceau, A.; Burghammer, M.; Lanson, B. *Chem. Mater.* **2003**, *15*, 4666–4678.

Table 2. EXAFS Best Fit Results of Hexagonal K$^+$-Birnessite

R	χ^2	f_{occ}	shell	CN	distance (Å)	σ^2 (Å^2)
0.0177	100.79	1.0	Mn^{4+}−O	6	1.90 (1)	0.001 (1)
		1.0	Mn^{3+}−O	6	2.19 (2)	0.002 (2)
		0.89 (3)	Mn^{4+}−Mn^{4+} edge	6	2.84 (3)	0.003 (1)
		1.0	Mn^{4+}−Mn^{3+} corner	0.8 (6)	3.43 (1)	0.017 (6)
		1.0	Mn^{4+}−O	6	3.40 (3)	0.002 (2)
		1.0	Mn^{4+}−O	12	4.60 (2)	0.005 (2)
		0.89 (3)	Mn^{4+}−Mn^{4+} (MS)	6	5.69 (2)	0.012 (2)

from temperature variable fits of β-MnO$_2$ spectra at 50, 100, 200, and 300 K and confirms literature values.[41] Single-scattering distances (R), Debye−Waller disorder parameter (σ^2), and layer-cation occupancy factor (f_{occ}) were varied freely, whereas Mn−Mn multiple-scattering distances were constrained to integral multiples of Mn−Mn single-scattering distances. Additional shells in the radial distribution function (RDF) were fit according to the crystal structure. Reported errors from curve-fit results in coordination numbers (N), scattering distance (R), and Debye−Waller parameter (σ^2) were derived by calculating the difference between the experimental spectra and least-squares fits.

A procedure for error estimation was required to test the validity of cation vacancy determination in layered MnO$_x$ compounds by direct comparison of Fourier transform moduli peak amplitudes. To this end, background spline polynomial functions, using AutoBK,[67] were removed from each individual spectrum, prior to averaging. The individual spectra were Fourier transformed, and the peak amplitudes were then measured. Figure 7 illustrates the relatively small 1σ amplitude deviations in the FT peak amplitudes for Ca$_2$Mn$_3$O$_8$ and ZnMn$_3$O$_7$ that were measured in transmission. Dilute samples of SP6-MnO$_x$ were measured in fluorescence yield mode, and amplitude deviations are greater than those measured in transmission. The error in f_{occ} was estimated by calculation of amplitude error bar limits. f_{occ} is reported as 0.88 ± 0.04, the mean of 0.87 ± 0.07 ($I_{Mn−Mn}/I_{Mn−O}$) and 0.89 ± 0.03 ($I_{MS}/I_{Mn−O}$). Despite large 1σ deviations in the SP6-MnO$_x$ EXAFS RDF peak amplitudes, relative to samples measured in transmission, the errors in f_{occ} are reasonable and demonstrate the validity and precision of this method.

Powder X-ray Diffraction (XRD). All synthetic MnO$_x$ standards were crushed in a mortar and pestle with ethanol. Samples were prepared by spreading powders onto a fused silica slide. Powder XRD patterns were collected using a Scintag XDS2000 diffractometer equipped with a Peltier cooled solid-state detector and a Cu Kα radiation source. A beam voltage of 40 kV and a 20 mA beam current were used. All diffractograms of reference compounds were collected at 0.05 °2θ/step for a duration of 1 s per step. The SP6-MnO$_x$ XRD pattern was collected at 0.05 °2θ/step for a duration of 12 s per step.

Results and Discussion

The structure of biogenic MnO$_x$ plays an important role in the fate, transport, and speciation of metals and organic matter in natural systems. The rate and kinetics of metal uptake into layered MnO$_x$ are governed by the distribution and quantity of excess surface charge. In layered MnO$_x$ excess negative charge can be created by the absence of layer cations (i.e., vacancies) and provides a driving force for cation sorption. Detailed hierarchical structure analysis of layered biogenic MnO$_x$, from local atomic structure to particle morphology, is crucial to gain a fundamental understanding of their properties and provide insight into their environmental role and potential application. Essential to the structure determination of biogenic MnO$_x$ on several length scales is a multitechnique approach that combines synthesis of model compounds with microscopy, spectroscopy, and diffraction.

Biogenic MnO$_x$ Particle Morphology. SP6-MnO$_x$ particles possess a fibrillar morphology with dimensions on the order of

~10 nm wide by ~100 nm long (Figure 1a). As the TEM stage is tilted from 0° to 30° the SP6-MnO$_x$ fibers become larger (Figure 1b). This indicates the possibility that SP6-MnO$_x$ particles resemble twisted sheets. Single MnO$_x$ layers with morphologies similar to that of SP6-MnO$_x$ recently were synthesized by surfactant exfoliation of crystalline birnessite and investigated by Ooi and co-workers.[74]

TEM images of hydrophilic resin embedded *L. discophora* SP6 and associated SP6-MnO$_x$ are shown in Figure 1a. Uranyl acetate stained samples illustrate that MnO$_x$ nucleation occurs on the exopolysacharide sheath which surrounds the bacterium, which is consistent with the observations of Ghiorse.[49,50] Nucleation of MnO$_x$ on the exopolysaccharide sheath (EPS) may indicate that a catalytically active functionality is present on the surface. The mechanism of bacterial Mn^{2+}$_{(aq)}$ oxidation remains an active area of research with important questions unanswered.[34,75] Structure determination of biogenic MnO$_x$ is one key parameter toward a comprehensive understanding of their formation as well as their environmental role.

X-ray Absorption Near Edge Spectroscopy (XANES). Given the existence of nearly 30 known MnO$_x$ mineral structures of different oxidation states, targeted syntheses of representative model compounds for comparison to the biogenic MnO$_x$ are challenging without *a priori* knowledge of the average oxidation state. Therefore, the first step taken toward structure elucidation was the determination of the average oxidation state and local coordination geometry of metal ions.

The XANES region of the X-ray absorption spectrum, approximately 100 eV below the ionization edge (Fermi energy), is particularly sensitive to average oxidation state, local coordination geometry, and resultant crystal field splitting.[76] In general, the energy of the X-ray absorption edge increases with increasing oxidation states as the successive removal of electrons from the absorbing atom raises the electron binding energy.[76] On the basis of calibration with MnO$_x$ standards with known oxidation states, the average oxidation state of manganese in SP6-MnO$_x$ was found to be 3.8 ± 0.3 (see Figure S1, Supporting Information), and manganese cations were found to be octahedrally coordinated. Local manganese coordination geometry and average oxidation state were ascertained by comparison of the SP6-MnO$_x$ XANES spectrum to abiotic reference standards with known oxidation states and crystal structures. An average oxidation state of 3.8 ± 0.3 indicates that SP6-MnO$_x$ consists primarily of Mn^{4+} with a fraction of manganese cations in a lower oxidation state.[14,71] The XANES spectrum of SP6-MnO$_x$ exhibits a double-hump feature in the pre-edge region, centered around 6540 and 6542 eV, that arises from bound state, quadrupole-allowed 1s to 3d transitions (Figure 2). A double-hump pre-edge resonance below the Mn K edge is characteristic of the octahedral crystal field splitting between e$_g$ and t$_{2g}$ orbitals.[71] As a result, Mn^{4+}O$_x$ with structures built from MnO$_6$ octahedra were synthesized as references for structure comparison with SP6-MnO$_x$ by EXAFS (Figure 3).

XANES was used as the principal means to characterize the average oxidation state and coordination geometry of manganese

(74) Yang, X. J.; Makita, Y.; Liu, Z. H.; Sakane, K.; Ooi, K. *Chem. Mater.* **2004**, *16*, 5581−5588.
(75) Webb, S. M.; Dick, G. J.; Bargar, J. R.; Tebo, B. M. *Proc. Natl. Acad. Sci. U.S.A.* **2005**, *102*, 5558−5563.
(76) Koningsberger, D. C.; Prins, R. *X-ray Absorption: Principles, Applications, Techniques of EXAFS, SEXAFS, and XANES*; Wiley: New York, 1988; pp XII, 673.
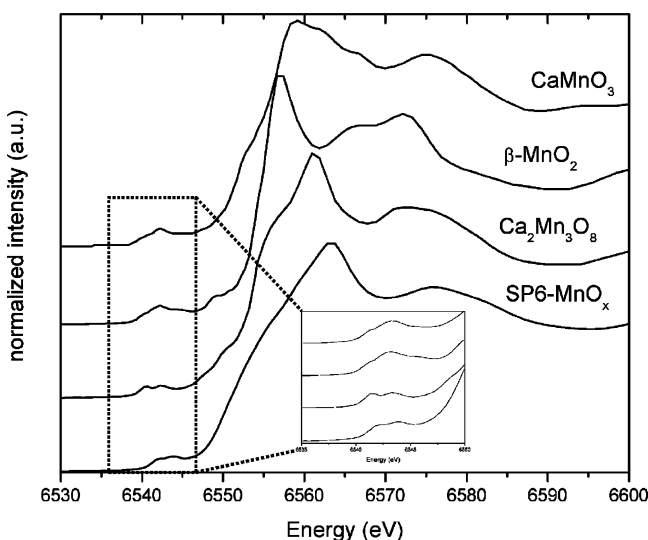
Figure 2. XANES comparison of SP6-MnO$_x$ with abiotic compounds. All compounds contain manganese in octahedral coordination environments. The double-hump feature in the pre-edge region arises from bound state, quadrupole-allowed 1s to 3d transitions. A double-hump pre-edge resonance below the Mn K edge is characteristic of the octahedral crystal field splitting between e$_g$ and t$_{2g}$ orbitals.
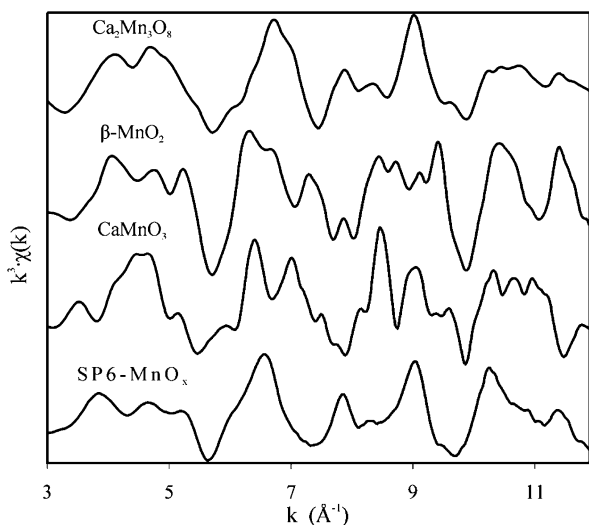
Figure 3. EXAFS spectroscopic comparison of MnO$_x$ compounds with different connectivities of MnO$_6$ octahedra. CaMnO$_3$ has a distorted perovskite structure made up entirely of corner-sharing MnO$_6$ octahedra. β-MnO$_2$ is isostructural with rutile and made up of both edge- and corner-sharing MnO$_6$ octahedra. Ca$_2$Mn$_3$O$_8$ is a layered structure and is composed of edge-sharing MnO$_6$ octahedra.

in samples maintained under natural, aqueous conditions. Note that a ∼10% error is associated with average oxidation state determination by XANES and is high relative to conventional reduction/oxidation titration techniques used to study oxides.[43] Redox titrations of environmental and biogenic samples are complicated by the presence of biological, organic, and inorganic substances, and it is often unclear whether the titrant solely oxidizes/reduces the material of interest and can produce erroneous results.

The EXAFS region of the X-ray absorption spectrum probes the average local environment around manganese up to approximately 6 Å and was used to qualitatively compare SP6-MnO$_x$ to model compounds that possess a variety of Mn^{4+}O$_6$ linkages, including all corner-sharing, all edge-sharing, and a combination of corner- and edge-sharing of octahedra (Figure 2). SP6-MnO$_x$ exhibits excellent qualitative spectral similarity with Ca$_2$Mn$_3$O$_8$ (Figure 2). Ca$_2$Mn$_3$O$_8$[57] is composed of edge-sharing Mn^{4+}O$_6$ octahedra that form layers. In contrast, CaMnO$_3$ is a distorted perovskite[77] composed of vertex-sharing Mn^{4+}O$_6$ octahedra. β-MnO$_2$ (pyrolusite) has a rutile-like structure[78] and is composed of both edge- and corner-sharing octahedra. Spectral similarity between the biogenic MnO$_x$ and Ca$_2$Mn$_3$O$_8$ implies that their local structures are closely related and indicates that SP6-MnO$_x$ is composed of edge-sharing MnO$_6$ octahedra that form into layers.

Structure Variations in Layered MnO$_x$. Layered MnO$_x$ are a diverse class of compounds with subtle differences that determine their bulk structure and properties.[31,79] Fundamentally, layered MnO$_x$ consist of infinite sheets of edge-sharing MnO$_6$ octahedra, analogous to the CdI$_2$ structure type. The oxidation state of layered manganese cations can be trivalent as in Cu$^+$-Mn^{3+}O$_2$,[80] all tetravalent as in Ca$_2$Mn$_3$O$_8$[57] and ZnMn$_3$O$_7$·3H$_2$O (Zn-chalcophanite),[81] or a mixture as in triclinic birnessite.[82] Layered MnO$_x$ often possess manganese cation vacancies within layers, as exemplified in Zn-chalcophanite[81] and Ca$_2$Mn$_3$O$_8$.[57]

The structure of Ca$_2$Mn$_3$O$_8$ was determined by single-crystal XRD[57] and provides a well-characterized, archetypal structure for spectroscopic comparison to biogenic MnO$_x$. Composed of infinite Mn$_3$O$_8$$^{4-}$ sheets held together by Ca^{2+} ions,[57] Ca$_2$Mn$_3$O$_8$ can be used as a model for layered MnO$_x$. Three-fourths of the available octahedral layer sites are occupied by Mn^{4+} in an ordered manner. The remaining one-fourth of the octahedral layer sites are vacant. Ca^{2+} ions occupy trigonal prismatic sites above and below layer vacancies to compensate for negative layer charge. This structural motif is common to anhydrous layered MnO$_x$ and has been shown in Co$_2$Mn$_3$O$_8$,[83,84] Mn^{2+}$_2$-Mn^{4+}$_3$O$_8$,[83,84] Cu$_2$Mn$_3$O$_8$,[85] and K$_2$Mn$_3$(OH)$_2$(VO$_4$)$_2$.[86] Similarly, ZnMn$_3$O$_7$·3H$_2$O is a hydrous layered Mn^{IV}O$_x$ in which one of seven (∼14.3%) Mn^{IV} layer cations are vacant.[81] Hydrated Zn^{2+} cations occupy trigonal sites above and below layer cation vacancies.[5,73,87]

Birnessites are a class of hydrous layered MnO$_x$ that are common throughout the natural environment.[31,88] Hexagonal birnessites contain variable quantities of Mn^{4+}, layer cation vacancies, and hydrated Mn^{3+} occupied sites above or below the vacancies. In hexagonal birnessites, electroneutrality is achieved by the presence of additional hydrated cations between adjacent layers, usually alkali or alkali earth metals. Attempts to determine the detailed structures of various birnessites have been complicated by low crystallinity and the inability to grow large single crystals. Over the past several years tremendous progress has been made in birnessite structure characterization

(77) Poeppelmeier, K. R.; Leonowicz, M. E.; Scanlon, J. C.; Longo, J. M.; Yelon, W. B. *J. Solid State Chem.* **1982**, *45*, 71−79.
(78) Baur, W. H. *Acta Crystallogr., Sect. B: Struct. Sci.* **1976**, *32*, 2200−2204.
(79) Suib, S. L. *Chem. Rev.* **1993**, *93*, 803−826.
(80) Topfer, J.; Trari, M.; Gravereau, P.; Chaminade, J. P.; Doumerc, J. P. *Z. Kristallogr.* **1995**, *210*, 184−187.
(81) Post, J. E.; Appleman, D. E. *Am. Mineral.* **1988**, *73*, 1401−1404.
(82) Lanson, B.; Drits, V. A.; Feng, Q.; Manceau, A. *Am. Mineral.* **2002**, *87*, 1662−1671.
(83) Oswald, H. R.; Feitknecht, W.; Wampetich, M. J. *Nature* **1965**, *207*, 72.
(84) Oswald, H. R.; Wampetich, M. J. *Helv. Chim. Acta* **1967**, *50*, 2023−2034.
(85) Riou, A.; Lecerf, A. *Acta Crystallogr., Sect. B: Struct. Sci.* **1977**, *33*, 1896−1900.
(86) Liao, J. H.; Guyomard, D.; Piffard, Y.; Tournoux, M. *Acta Crystallogr., Sect. C: Cryst. Struct. Commun.* **1996**, *52*, 284−286.
(87) Gaillot, A. C.; Drits, V. A.; Plancon, A.; Lanson, B. *Chem. Mater.* **2004**, *16*, 1890−1905.
(88) Post, J. E.; Veblen, D. R. *Am. Mineral.* **1990**, *75*, 477−489.

and classification of their numerous structure variations.[73,82,87,89,90] The work of Lanson[73,82,87,89,90] and Wang[48,91] has proven to be seminal to the structure determination of biogenic MnO_x and facilitated the first complete structure determinations of biogenic MnO_x formed by *Pseudomonas putida* strain MnB1[43] and *Bacillus* sp. strain SG1.[41]

Qualitative Comparison of Abiotic Layered MnO_x with Biogenic MnO_x. Figure 4 presents the EXAFS spectra of SP6-MnO_x, several layered MnO_x structures, and one tunnel-type MnO_x structure and provides a comparison of their local structures. The local manganese environment in SP6-MnO_x is qualitatively similar to layered H^+-birnessite, K^+-birnessite, Zn-chalcophanite, and $Ca_2Mn_3O_8$ as evidenced by its EXAFS spectrum.

Figure 4 demonstrates that the spectrum of Mg-OMS1 is significantly different from that of SP6-MnO_x. Mg-OMS1[11] is a synthetic analogue of todorokite[92] with a 3 × 3 tunnel-type structure and was included in this study because Kim and co-workers[44,45] recently reported that SP6-MnO_x closely resembles a todorokite-like mineral. Kim et al. used UV Raman vibrational spectroscopy and EXAFS to compare SP6-MnO_x to several natural MnO_x mineral samples.[44,45] The use of natural MnO_x minerals as XAS reference standards is challenging owing to the common presence of several phases within one sample. Kim et al.[44] do not provide evidence that mineral samples used as XAS reference standards were monophasic. In addition, the poor quality of their EXAFS data did not allow detailed spectral analysis. We demonstrate that the EXAFS spectra of SP6-MnO_x and phase pure, synthetic todorokite (Mg-OMS1) differ, particularly in the region $7.5 \text{ Å}^{-1} \leq k \leq 9.5 \text{ Å}^{-1}$ (Figure 3). Navrotsky and co-workers have demonstrated by calorimetry that the thermodynamic stability of layered MnO_x phases depends largely on the specific type and number of interlayer cations and the degree of hydration.[47] Therefore, given small energetic differences (~30 kJ/mol) between metastable layered and tunnel-type MnO_x,[47] even investigation under low laser power may induce local heating[93] and phase transformation. In their study, Kim et al.[44,45] based their structural study on UV Raman laser spectroscopy as the XAS data were not conclusive. The possibility of local phase transformation through laser-induced heating of layered MnO_x appears to be likely and is further supported by the fact that the synthesis of todorokite-like structures (e.g., Mg-OMS1) proceeds by low-temperature hydrothermal treatment of layered precursors.[71,94,95] Moreover, Figure 9 reveals that the peak positions in the XRD pattern of Mg-OMS1 do not match that of the biogenic oxide, consistent with different bulk structures. Consequently, we do not believe that SP6-MnO_x has a todorokite-like tunnel structure under environmentally relevant conditions, and the remainder of the structure determination focuses on comparisons with layered structures.
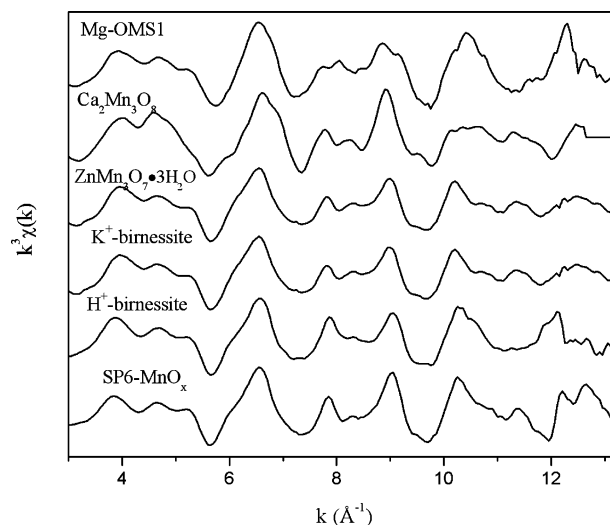
(89) Drits, V. A.; Silvester, E.; Gorshkov, A. I.; Manceau, A. *Am. Mineral.* **1997**, *82*, 946−961.
(90) Lanson, B.; Drits, V. A.; Silvester, E.; Manceau, A. *Am. Mineral.* **2000**, *85*, 826−838.
(91) Yang, X.; Tang, W.; Feng, Q.; Ooi, K. *Cryst. Growth Des.* **2003**, *3*, 409−415.
(92) Post, J. E.; Bish, D. L. *Am. Mineral.* **1988**, *73*, 861−869.
(93) Haro-Poniatowski, E.; Julien, C.; Pecquenard, B.; Livage, J.; Camacho-Lopez, M. A. *J. Mater. Res.* **1998**, *13*, 1033−1037.
(94) Brock, S. L.; Sanabria, M.; Suib, S. L.; Urban, V.; Thiyagarajan, P.; Potter, D. I. *J. Phys. Chem. B* **1999**, *103*, 7416−7428.
(95) Luo, J.; Zhang, Q. H.; Huang, A. M.; Giraldo, O.; Suib, S. L. *Inorg. Chem.* **1999**, *38*, 6106−6113.
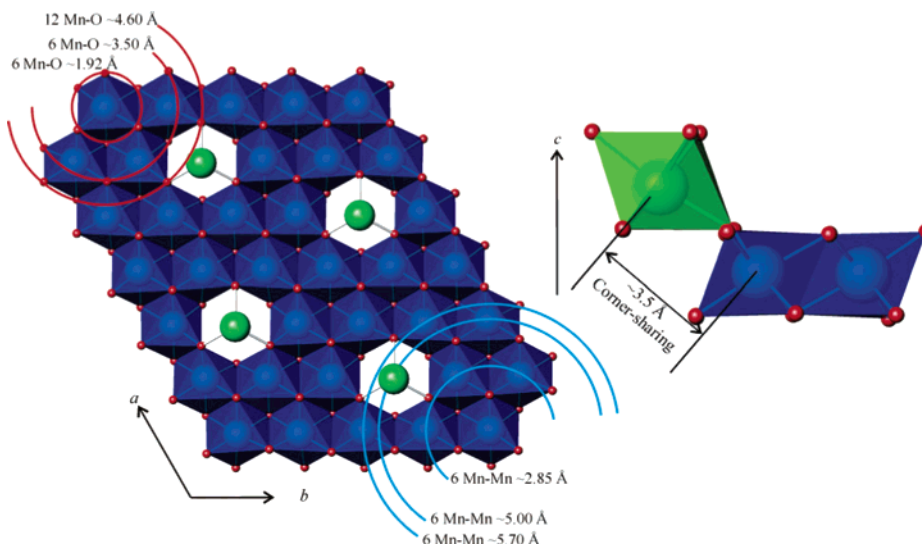
Figure 4. EXAFS comparison of biogenic MnO_x with abiotic layered and one tunnel-type MnO_x. Mg-OMS1 is a synthetic todorokite with a 3 × 3 tunnel framework structure.

A high degree of qualitative similarity was observed in the EXAFS spectra of biogenic MnO_x, hexagonal birnessites, Zn-chalcophanite, and $Ca_2Mn_3O_8$ (Figure 4). Each abiotic reference MnO_x example represents a different fraction of cation vacancies, degree of interlayer hydration, or stacking pattern of adjacent layers as summarized in Table 1. The structures of Zn-chalcophanite, hexagonal birnessite, and $Ca_2Mn_3O_8$ are closely related. Most significant in terms of the short-range structure are variations in the number of layer cation vacancies between these three structures. The percentage of cation vacancies varies from approximately 12% in hexagonal K^+-birnessite[73] to 14.3% in $ZnMn_3O_7 \cdot 3H_2O$[81] to 25% in $Ca_2Mn_3O_8$.[57] Given the spectral similarities between these three layered MnO_x structures, the layer structure of K^+-birnessite was chosen as our structural model (Figure 5) as its complete structure has been determined recently by EXAFS and XRD.[41,73]

Biogenic MnO_x Curve Fit. The model used to fit the K^+-birnessite EXAFS spectrum is illustrated in Figure 5, the best fit is illustrated in Figure 6, and best fit results are summarized in Table 2. Best fit values from EXAFS match crystallographic interatomic distances to within ±0.02 Å. The model used to fit the K^+-birnessite spectrum was validated by successful application to the EXAFS spectra of nearly isomorphic H^+-birnessite and Zn-chalcophanite. The local structure of SP6-MnO_x was determined by fitting the K^+-birnessite structure model to the biogenic MnO_x EXAFS spectrum (Figure 7; Table 3).

The first Mn−O shell was fit with six oxygen backscatterers at a distances of 1.89 Å (layer Mn^{4+}−O) and 2.14 Å (interlayer Mn^{3+}−O). The second shell was fit with six Mn−Mn scattering paths at a distance of 2.85 Å, representative of edge-sharing MnO_6 octahedra with hexagonal layer symmetry. The coordination number for nearest-neighbor Mn^{4+} cations at 2.85 Å was multiplied by an occupancy factor (f_{occ}) to account for cation vacancies. The third shell was fit with a Mn−Mn path at 3.45 Å, representative of corner-sharing octahedra, and six Mn−O paths at a similar distance. The Mn^{4+}−Mn^{3+} coordination number was allowed to float, whereas the Mn−O coordination number was fixed to six. The number of Mn^{4+}−Mn^{3+} paths should be equivalent to the number of cation vacancies ($1 - f_{occ}$), a relatively small fraction of the total number of layer

Figure 5. General layer model used to fit the SP6-MnO$_x$ EXAFS spectrum. Model is based on K$^+$-birnessite. The hexagonal layer slab is composed of edge-sharing Mn^{4+}O$_6$ octahedra (blue). A fraction of the layer Mn^{4+} cations are vacant, resulting in a negatively charged layer. Mn^{3+} cations (green) occupy sites above/below the Mn^{4+} layer vacancies.

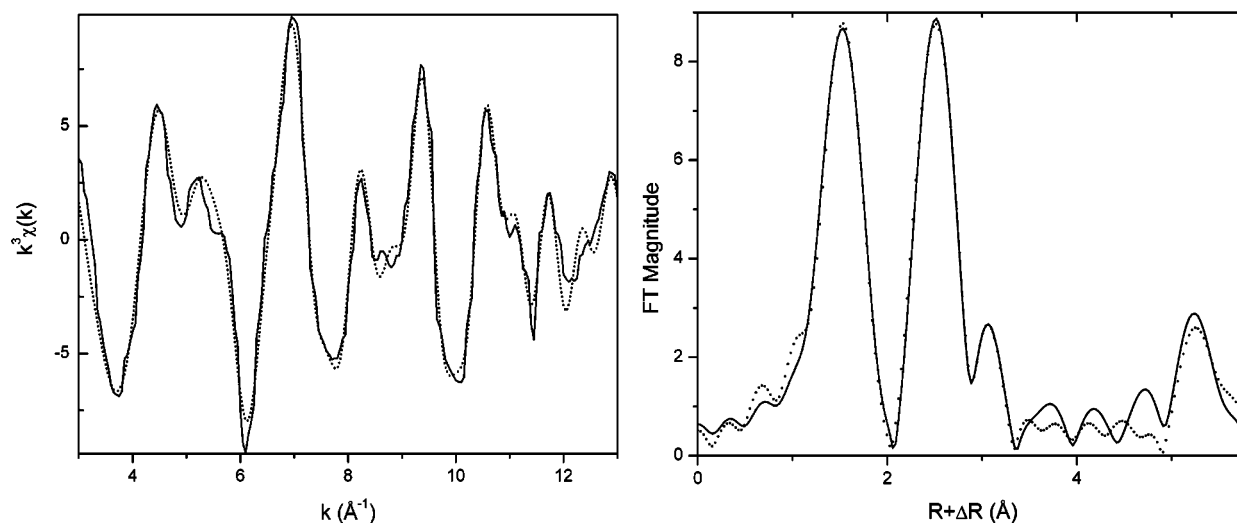**Figure 6.** Best fit of the hexagonal K$^+$-birnessite model EXAFS spectrum: (a) EXAFS of c-ordered hexagonal birnessite (solid line) with best fit overlay (dotted line); (b) Fourier transformed EXAFS spectrum of c-ordered hexagonal birnessite (solid line) with best fit overlaid (dotted line).

cations. Fitting the low-amplitude, broad shell at 3.45 Å with two different scattering atoms at similar distances (six Mn−O and Mn^{4+}−Mn^{3+}) is difficult and results in a Mn^{3+}−Mn^{4+} fit coordination number value of less than one and a Debye−Waller factor (σ^2) that is an order of magnitude larger than edge-sharing Mn^{4+}−Mn^{4+} paths. MS paths centered around 5 Å were best fit by constraining path distances to integral multiples of Mn−Mn single-scattering paths with scattering angles of 180°, indicating linear layers along [100] and [010] crystallographic directions (Figure 5). The MS path coordination numbers were constrained by multiplication of six backscattering atoms with f_{occ} to account for cation vacancies. Best fit results are shown in Figure 6 and summarized in Table 2 and illustrate that physical parameters coincide with the crystallographic inter-atomic distances.

In hexagonal K$^+$-birnessite, approximately 12% of Mn^{4+} cations are absent within the layers.[73,87] The absence of layer cations causes an amplitude reduction in the EXAFS spectrum for all Mn−Mn single- and multiple-scattering paths at or integer multiples of distances representative of edge-sharing MnO$_6$

octahedra, at approximately 2.85 Å. Accounting for cation vacancies is accomplished with the use of a few physically realistic approximations, as demonstrated by Ressler et al.[71] and Webb et al.[41] In the EXAFS equation two multiplicative terms describe the spectral amplitude, the amplitude reduction factor, S_0^2, and coordination number, N, at distance R from the absorbing atom. S_0^2 is the amplitude reduction factor and is a constant characteristic of the absorbing atom. Therefore, cation vacancies will reduce the observed coordination number (N) at distance R from the absorbing atom. The cation vacancies in biogenic MnO$_x$ and abiotic model compounds were accounted for by constraining S_0^2 to 0.83, $\Delta E_0 = 0$, and coordination numbers (N) to their crystallographic values, while allowing a multiplicative fractional occupancy parameter (f_{occ}) to vary freely.[41] Our model was based on the conceptual framework of Ressler et al.[71] Its importance has been demonstrated elegantly in the identification of the biogenic MnO$_x$ phase formed by the marine *Bacillus* sp. strain SG-1 by Webb and co-workers.[41]

Quantitative Analysis of Cation Vacancies by EXAFS. Quantitative analysis of cation vacancies in poorly crystalline,
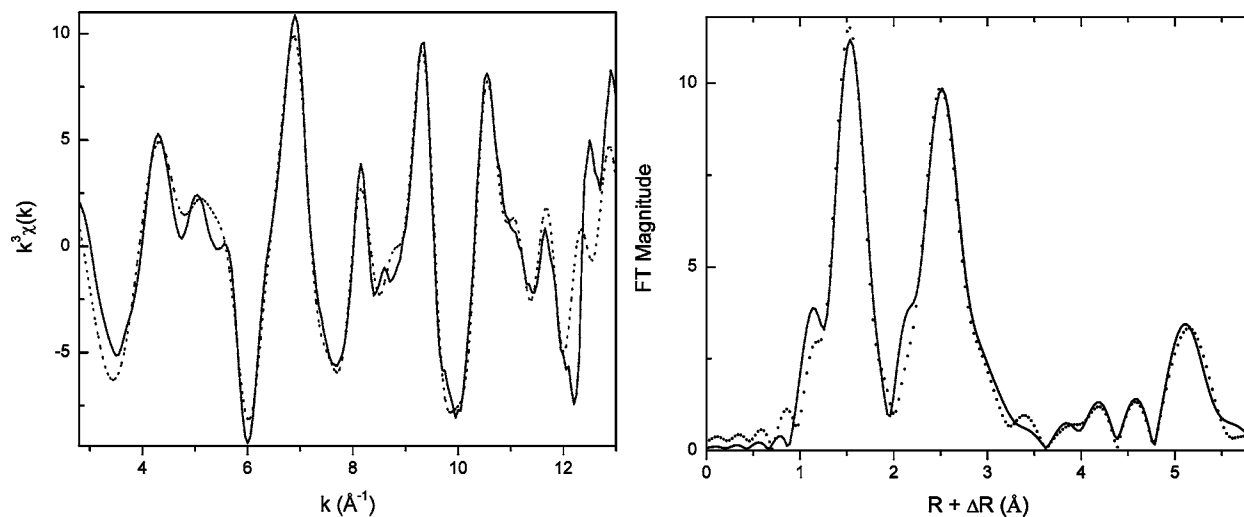
Figure 7. Best fit of the SP6-MnO$_x$ EXAFS spectrum: (a) EXAFS of biogenic MnO$_x$ (solid line) with best fit overlay (dotted line); (b) Fourier transformed EXAFS spectrum of SP6-MnO$_x$ (solid line) with best fit overlaid (dotted line).

Table 3. EXAFS Best Fit Results of the SP6-MnO$_x$ Local Structure

R	χ^2	f_{occ}	shell	CN	distance (Å)	σ^2 (Å^2)
0.0156	296.25	1.0	Mn^{4+}–O	6	1.89 (1)	0.001 (2)
		1.0	Mn^{3+}–O	6	2.14 (3)	0.002 (2)
		0.88 (3)	Mn^{4+}–Mn^{4+} edge	6	2.86 (1)	0.003 (1)
		1.0	Mn^{4+}–Mn^{3+} corner	0.8 (6)	3.43 (2)	0.016 (6)
		1.0	Mn^{4+}–O	6	3.41 (3)	0.003 (2)
		1.0	Mn^{4+}–O	12	4.61 (6)	0.005 (2)
		0.88 (3)	Mn^{4+}–Mn^{4+} (MS)	6	5.72 (2)	0.012 (2)
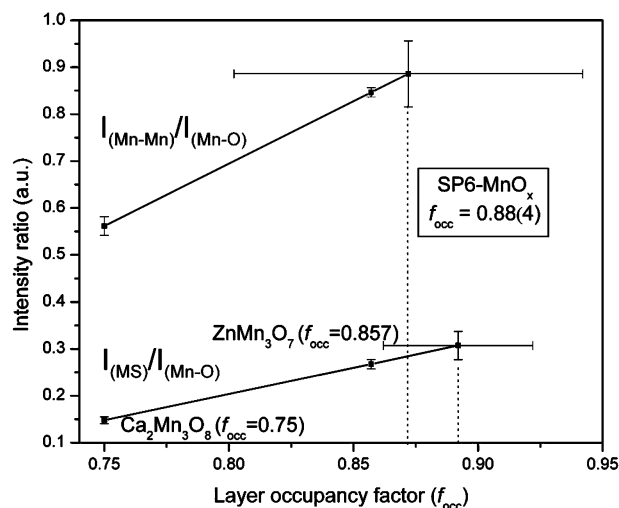
Figure 8. Quantification of layer cation occupancy (f_{occ}). Peak intensities of Mn–Mn single-scattering and Mn–Mn (MS) multiple-scattering paths were normalized by the intensity of the Mn–O peak. The SP6-MnO$_x$ layer has a Mn^{4+} cation occupancy of 0.88 ± 0.04.

layered MnO$_x$ by EXAFS is feasible and demonstrated below (Figure 8). ZnMn$_3$O$_7$·3H$_2$O and Ca$_2$Mn$_3$O$_8$ contain ordered and stoichiometric quantities of layer cation vacancies and are excellent standards for the quantification of cation vacancies in environmental and nanocrystalline materials.

In accordance with the Beer–Lambert law, absorbance increases (decreases) proportionally with concentration (vacancies). Therefore, it is expected that the RDF peak amplitudes of single- and multiple-scattering paths associated with Mn–Mn edge-sharing octahedra decrease with increasing layer cation vacancies. Theoretical EXAFS calculations made on a K$^+$-

birnessite model with various numbers of vacancies demonstrate the inverse proportionality between the number of cation vacancies and RDF peak amplitudes (see Figure S5, Supporting Information). This linear relationship between RDF peak amplitude and f_{occ} provides a basis for calibration of cation vacancies with the use of well-characterized, layered MnO$_x$ reference materials. Analysis of cation vacancies based on Fourier transform (FT) moduli is possible only among materials that are structurally similar on the scale probed by EXAFS and assumes that the σ^2 and S_0^2 are the same and $\Delta E_0 = 0$. Therefore, changes in the second shell (Mn^{4+}–Mn^{4+}) and MS shell RDF peak amplitudes result from changes in the number of atoms that give rise to those peaks. This affords a direct comparison of cation vacancies in layered MnO$_x$ compounds.

Figure 8 illustrates cation vacancy calibration curves using single- and multiple-scattering FT moduli amplitudes from the EXAFS spectra of ZnMn$_3$O$_7$·3H$_2$O ($f_{occ} = 0.857$) and Ca$_2$Mn$_3$O$_8$ ($f_{occ} = 0.75$). Owing to small variations in Mn–Mn single- (2.85 Å) and multiple-scattering (5.7 Å) peak intensities between the RDF spectra of each reference compound, their intensities were normalized with respect to the intensity of the Mn–O peak (~1.92 Å) in each spectrum. Normalization of Mn–Mn peaks, by division of the Mn–O peak intensity, affords interspectral comparison. Therefore, the intensity ratios of $I_{Mn–Mn(2.85 \text{ Å})}/I_{Mn–O}$ and $I_{MS(5.7 \text{ Å})}/I_{Mn–O}$ are plotted in Figure 8. On the basis of the calibration of cation vacancies in layered MnO$_x$, SP6-MnO$_x$ contains 12 ± 4% layer cation vacancies and is similar to hexagonal birnessite and ZnMn$_3$O$_7$·3H$_2$O (Zn-chalcophanite). The layer structures of c-ordered hexagonal birnessite and Zn-chalcophanite are structurally similar, containing ~12% and ~14% layer cation vacancies, respectively. Hydrated interlayer Mn^{3+} and metal cations compensate for the negative layer charge in hexagonal birnessites, whereas in ZnMn$_3$O$_7$·3H$_2$O hydrated Zn^{2+} cations compensate for vacant Mn^{4+} layer cations. Therefore, on the basis of the number of cation vacancies, the biogenic MnO$_x$ possesses a structure similar to hexagonal birnessite and Zn-chalcophanite. Because biogenic MnO$_x$ contains Mn^{3+} cations above/below layer cation vacancies, it belongs to the hexagonal birnessite family of compounds.

Similar analyses of EXAFS peak intensities have been demonstrated in site occupancy determination of cations in

spinel ferrite nanoparticles.[96,97] The calibration of cation vacancies in layered oxides has never been directly demonstrated previously. The quantification of cation vacancies in noncrystalline materials is extremely desirable as they play an important role in the determination of catalytic and cation-exchange properties.

Local Structure of Biogenic MnO$_x$. The best fit of the biogenic MnO$_x$ spectrum (Figure 7; Table 3) indicates that its structure consists of symmetrical edge-sharing MnO$_6$ octahedra which form two-dimensional layers that closely resemble hexagonal birnessite. The best fit of the SP6-MnO$_x$ EXAFS spectrum converged with goodness-of-fit parameters $R = 0.0156$ and $\chi^2 = 296.25$. Detailed analysis of the EXAFS spectrum indicates that $12 \pm 4\%$ of the Mn^{4+} layer cation sites in SP6-MnO$_x$ are vacant, whereas the analysis of the XANES suggests that the average oxidation state of Mn is 3.8 ± 0.3. Therefore, the average chemical formula of SP6-MnO$_x$ is M$^{n+}_y$Mn$^{3+}_{0.12}$[$\square_{0.12}$Mn$^{4+}_{0.88}$]O$_2 \cdot z$H$_2$O, where M$^{n+}_y$ and Mn$^{3+}_{0.12}$ represent hydrated interlayer cations and $\square_{0.12}$ represents the number of cation vacancies within the layer. Adjacent layers in hydrous layered MnO$_x$ are typically at least 7 Å apart and cannot be interrogated by EXAFS. Consequently, powder XRD was used to investigate the long-range stacking relationship between adjacent layers.

Powder XRD: Long-Range, Bulk Structure. The long-range structure of hexagonal birnessites is delineated according to the degree of ordering along the layer stacking axis (usually the c-axis).[90] Hexagonal birnessites are either ordered or disordered along the c-axis and are referred to as "c-ordered" or "c-disordered" hexagonal birnessite, respectively. δ-MnO$_2$ represents the most extreme case of c-disordering and is essentially single layered with hexagonal symmetry. Polymorphs of hexagonal birnessite are readily distinguishable by the relative intensities of 00l reflections measured by powder X-ray. The relative intensities of 00l reflections vary with the degree of stacking order/disorder along the c-axis.[87]

L. discophora SP6 produces a MnO$_x$ that either is composed of single layers similar to δ-MnO$_2$ or has poorly ordered stacking of adjacent layers similar to H$^+$-birnessite. To isolate Bragg diffraction peaks that arise from the biogenic MnO$_x$, XRD patterns of SP6 cells with *and* without MnO$_x$ were collected (see Figure S6, Supporting Information). Scattering from SP6-MnO$_x$ gives rise to two asymmetric peaks centered at $d \sim 2.5$ Å and ~ 1.45 Å (Figure 9). A comparison of the powder XRD patterns of hexagonal birnessites and Mg-OMS1 with SP6-MnO$_x$ clearly demonstrates that their long-range structures are different from that of Mg-OMS1 and confirms local differences seen by EXAFS. The hexagonal birnessite structure was used to index the two asymmetric XRD peaks in SP6-MnO$_x$ because their local structures are similar according to EXAFS.

The powder XRD patterns of K$^+$-birnessite and H$^+$-birnessite (Figure 9) are indexed with a hexagonal unit cell (P 6$_3$/mmc, $a = 2.840$ Å, $c = 14.50$ Å).[73] The XRD pattern of K$^+$-birnessite exhibits sharp 00l reflections, indicative of relatively ordered layers. In comparison, the XRD patterns of H$^+$-birnessite and SP6-MnO$_x$ demonstrate relatively disordered stacking of adjacent layers, as illustrated by weak or absent 00l reflections.
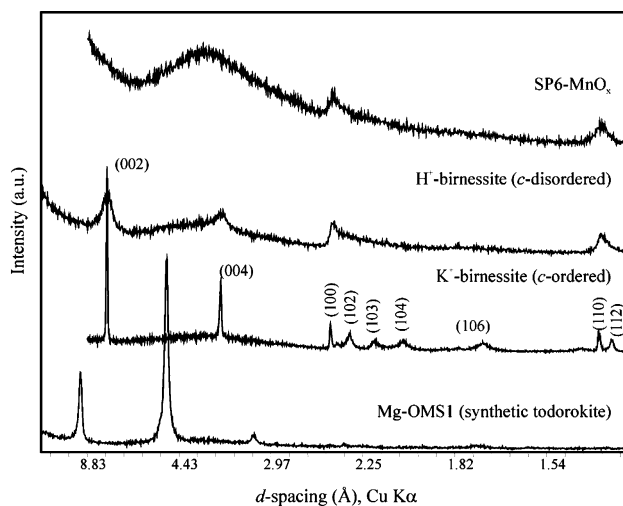

Figure 9. Comparison of biogenic MnO$_x$ with model compounds by powder XRD. SP6-MnO$_x$ most closely resembles c-disordered hexagonal birnessite, indicating a layered MnO$_x$ with poorly crystalline stacking along the c-axis. The diffraction patterns of hexagonal birnessites are indexed with a hexagonal cell (P 6$_3$/mmc, $a = 2.840$ Å, $c = 14.50$ Å, $\alpha = 90°$ $\beta = 90°$ $\gamma = 120°$). Note the similarity between the powder XRD patterns of SP6-MnO$_x$ and c-disordered hexagonal birnessite.

However, the XRD patterns of H$^+$-birnessite and biogenic MnO$_x$ exhibit $h00$ and $hk0$ peaks that arise from layers.

The two asymmetric peaks in the powder XRD pattern of SP6-MnO$_x$ centered around $d \sim 2.5$ Å and ~ 1.45 Å correspond to the (100) and (110) reflections that result from the ab-layer plane. Owing to background scatter from biological and organic media, weak $00l$ reflections may be hidden, and it is not possible to determine whether biogenic MnO$_x$ consists of discrete layers, as in the case of δ-MnO$_2$, or poorly ordered stacking of adjacent layers, as in H$^+$-birnessite.

Conclusions

Microorganisms accelerate aqueous Mn^{2+} oxidation up to five orders of magnitude relative to abiotic processes.[34,36,98] The mechanism of aqueous Mn^{2+} oxidation and extracellular MnO$_x$ formation by microorganisms is not yet understood, although several studies are ongoing.[33,75,99−105] Structure determination of biogenic MnO$_x$ is an important step toward a comprehensive understanding of their role in natural systems. In this study, a combination of TEM, XAS, and XRD was used to determine the morphology and local and long-range structure of the biogenic MnO$_x$ precipitate formed by the freshwater bacterium *L. discophora* SP6. The bacteria form a mixed-valent, layered MnO$_x$ with an average chemical formula of M$^{n+}_y$Mn$^{3+}_{0.12}$[$\square_{0.12}$Mn$^{4+}_{0.88}$]O$_2 \cdot z$H$_2$O. This work demonstrates that the biogenic

(96) Yang, A.; Harris, V. G.; Calvin, S.; Zuo, X.; Vittoria, C. *IEEE Trans. Magn.* **2004**, *40*, 2802−2804.

(97) Calvin, S.; Carpenter, E. E.; Harris, V. G.; Morrison, S. A. *Appl. Phys. Lett.* **2002**, *81*, 3828−3830.

(98) Nealson, K. H.; Tebo, B. *Origins Life* **1980**, *10*, 117−126.

(99) Brouwers, G.-J.; De Vrind, J. P. M.; Corstjens, P. L. A. M.; Cornelis, P.; Baysse, C.; De Vrind-De Jong, E. W. *Appl. Environ. Microbiol.* **1999**, *65*, 1762−1768.

(100) Brouwers, G. J.; Corstjens, P. L. A. M.; De Vrind, J. P. M.; Verkamman, A.; De Kuyper, M.; De Vrind-De Jong, E. W. *Geomicrobiol. J.* **2000**, *17*, 25−33.

(101) Brouwers, G. J.; Vijgenboom, E.; Corstjens, P. L. A. M.; De Vrind, J. P. M.; De Vrind-De Jong, E. W. *Geomicrobiol. J.* **2000**, *17*, 1−24.

(102) Francis, C. A.; Tebo, B. M. *Appl. Environ. Microbiol.* **2001**, *67*, 4272−4278.

(103) Francis, C. A.; Casciotti, K. L.; Tebo, B. M. *Arch. Microbiol.* **2002**, *178*, 450−456.

(104) Francis, C. A.; Tebo, B. M. *Appl. Environ. Microbiol.* **2002**, *68*, 874−880.

(105) Miyata, N.; Tani, Y.; Iwahori, K.; Soma, M. *FEMS Microbiol. Ecol.* **2004**, *47*, 101−109.

MnO_x layer structure is very similar to hexagonal birnessites,[73,74,87,90] Zn-chalcophanite,[58,81] and $Ca_2Mn_3O_8$.[57] Nearly identical structures have recently been reported as the oxide products produced by other phylogenetically diverse manganese oxidizing bacteria, such as the spore-forming marine *Bacillus* sp. strain SG1[41] and *P. putida* strain MnB1.[43] The ability of microorganisms to catalytically oxidize Mn^{2+} is linked to the presence of genes that express extracellular multicopper oxidases.[75,99,101,102] The formation of isomorphic MnO_x products formed by otherwise phylogenetically distinct bacteria that live in diverse environments provides important insight into their formation. Specifically, biogenic formation of poorly crystalline, layered manganese oxides likely proceeds without biological templating or direct control by the microorganism.

Supporting Information Available: The XANES spectrum of SP6-MnO_x, average manganese oxidation state calibration curve, X-ray absorption spectra and fits of $ZnMn_3O_7 \cdot 3H_2O$ and $Ca_2Mn_3O_8$, EXAFS model validation, theoretical calculation of EXAFS as a function of cation vacancies, and powder XRD patterns of *Leptothrix discophora* SP6. This material is available free of charge via the Internet at http://pubs.acs.org.

JA062097G